

1 An investigation into the spectral parameters of ULF waves in the 2 polar caps and magnetotail

3 Nataliya Sergeevna Nosikova^{1,2}, Nadezda Viktorovna Yagova², Lisa Jane Baddeley³, Dag Arne
4 Lorentzen³, Dmitriy Anatolyevich Sormakov⁴

5 ¹National Nuclear University “MEPhI”, Moscow, Russia

6 ² Schmidt Institute of Physics of the Earth of the Russian Academy of Sciences (IPE RAS), Moscow, Russia

7 ³University Center on Svalbard, Norway

8 ⁴Arctic and Antarctic Research Institute, AARI, Geophysics department, Sankt-Petersburg, Russia

9 *Correspondence to:* Nataliya S Nosikova (NSNosikova@mephi.ru)

10 **Abstract.**

11 The present case study is focused on fluctuations at \sim 1.5 mHz observed at open field lines, in the both polar caps in ground-
12 based geomagnetic data and in electron concentration in the northern hemisphere ionosphere. Coherent pulsations with a
13 relatively narrow Pc-like spectra and a higher fraction of the transversal components in the total spectral power are also
14 observed by the Cluster satellites in the magnetotail magnetic field. Interestingly, the pulsations in the magnetotail started after
15 pulsations over a similar frequency range observed in the solar wind dynamic pressure and IMF had been switched off. This
16 suggests evidence of an internal, resonant magnetotail mode which is normally masked by a higher amplitude broadband ULF
17 “noise” of extra-magnetospheric origin.

18 **1 Introduction**

19 One of the most important mechanism of energy transfer in the Magnetosphere is through the propagation of Ultra Low
20 Frequency (ULF) waves. Of particular interest are intensive, high latitude geomagnetic pulsations at mHz frequencies
21 (Pc5/Pi3). These pulsations are the most long-period and intensive magneto-hydrodynamic (MHD) waves in the
22 magnetosphere. Their longest possible period is determined by the magnetosphere size to Alfvén velocity ratio and is about
23 10^3 s. Contribution of ULF waves into the solar-wind magnetosphere interaction is quantified by ULF wave indexes (e.g.
24 Kozyreva et al., 2007, Borovsky and Denton, 2014). The highest Pc5/Pi3 amplitudes correspond to auroral latitudes (Baker et
25 al., 2003). Specific ULF activations were found near the polar boundary of the auroral oval and associated with polar boundary

intensifications (PBIs) (Lyons et al., 1999). The other region of high Pi3 intensities is collocated with the cusp/cleft region (Bolshakova and Troitskaya, 1977; De Lauretis et al., 2016). Meanwhile, Pc5/Pi3 are observed in the polar caps, where field lines are “open”. They are characterized by lower amplitudes (in comparison to auroral Pc5 pulsations which can result from Alfvén field-line resonance (FLR) on closed field lines) and are more irregular with typically lower central frequencies \sim a few mHz (Bland and McDonald, 2016). A detailed analysis of morphological properties of these pulsations can be found in (Yagova et al., 2004; Francia et al., 2005). These pulsations are simultaneously seen in geomagnetic and radar data and might be directly driven by perturbations in the SW, be related to substorms or be a result of internal processes in the magnetosphere. The polar cap pulsations are coherent at long distances (Yagova et al., 2004). This indicates that an external source of these pulsations should exist. Kepko et al. (2002) suggested that the primary cause of global magnetospheric pulsations is ULF perturbations in the pressure and density of the Solar Wind (SW). In some cases, these pulsations are literally global. Thus Han et al. (2007) reported on low latitude observations of global Pi3 pulsations directly driven by fluctuations in the SW. A contribution of the main SW/IMF pulsations to the spectral power of polar cap Pi3s was estimated by Yagova et al. (2007) who showed that the amplitudes of polar cap Pi3s and fluctuations of IMF SW dynamic pressure in the same frequency range correlate not only for high amplitude wave packets but at any intensity of extra-magnetospheric fluctuations. Later, Kepko et al. (2020) carried out a detailed analysis of long-term observations of quasi-periodical spatial mesoscale irregularities in the SW number density. The authors have shown that at least some of the frequencies of global pulsations in mHz range can originate from the meso-scale SW structures. If the ULF variations in the SW are neglectable, pulsations might result from exciting Kelvin-Helmholtz instability in the magnetosphere (Mann et al., 2002, Rae et al., 2005, Keiling 2009).

Inside the magnetosphere, the spectral parameters of ULF waves can be determined by spectral characteristics of disturbances outside the magnetosphere along with the waveguide and resonance properties of the magnetosphere-ionosphere system (e.g., Alperovich and Fedorov, 2007). In particular, it has been shown that ULF spectra at polar cap latitudes are not totally controlled by the parameters in front of the bow shock but are a manifestation of processes in the magnetosphere and magnetosheath (Yagova, 2015). Pilipenko et al. (2005) theoretically showed, that an Alfvén quasi-resonator can be formed on open field lines due to the curvature of the magnetic field. This mechanism can provide one explanation ULF activity observed in the polar cap.

As polar caps are projections of the geomagnetic tail lobes, existence of specific tail modes was discussed by (Allan and Wright, 2000). Cluster observations showed low average amplitudes of ULF in the tail lobes, as well as weak correlation of ULF power in both Pi2 and Pc5 frequency bands with auroral activity (Wang et al., 2016). Zhang et al. (2018) used ion velocity data to identify ULF waves and analyzed how substorm activity influences wave occurrence and the main frequency. They found that the Pc5 frequencies differ for non-substorm and substorm waves. Ballatore (2003) analyzed statistically integral parameters of ULF power in Pc5 range at two nominally conjugated positions. In both papers mentioned above there was no information about pulsation waveforms or coherence. An important evidence of interrelation between ULF activity in the polar cap and at auroral latitudes was found by (Bland and McDonald, 2016) who studied high latitude ULF waves under

59 quiet geomagnetic conditions. The authors found that polar cap ULF waves were accompanied by simultaneous activity in the
60 dayside auroral zone at nearly the same frequency (1-1.3 mHz).

61 However, there are only a few publications on conjugated observations of ULF waves in the magnetotail and one or
62 both polar caps or between two hemispheres at cap latitudes. This is partly because of low amplitudes of polar cap Pi3s which
63 are usually masked by more intensive directly driven fluctuations seen simultaneously throughout the high latitude region.
64 The other source of contamination is associated to PBIs (Lyons et al., 1999; 2011). The inter-relations between the auroral
65 activations, PBIs and auroral phenomena in the polar caps was studied by Nishimura et al. (2013; 2014). Although a substorm
66 is mostly an auroral phenomena, it causes essential changes in/across the whole night-time magnetosphere and is followed by
67 auroral and geomagnetic disturbances in the polar caps. The oscillations in the Pc5/Pi3 range caused by a substorm in polar
68 cap particle precipitation was reported in (Weatherwax et al., 1997). Pre-substorm variations of polar cap ULF activity were
69 reported in (Heacock and Chao, 1980; Yagova et al, 2000; 2017). Shi et al. (2018) summarized previous studies of long-lasting
70 poloidal ULF waves in the Magnetosphere including their own investigation. It is seen from Table 1 in (Shi et al., 2018) that
71 the mean duration of the event is 2-3 days, and pulsations are detected on the dayside or from the dayside to midnight. The
72 authors pointed out that “the waves were usually monochromatic and observed during low geomagnetic activity after a
73 geomagnetic storm or within the storm recovery phase”. Later, (Shi et al., 2020) concentrated on one event from those studied
74 in (Shi et al., 2018). The authors reported long-lasting Pc5 pulsations from L~5.5 and up to the polar caps in both hemispheres
75 seen simultaneously in the ground-based magnetometer and SuperDARN radar data. At the same time, pulsations were
76 detected by MMS satellite in the Magnetosphere. Their study indicated that the Pc5 pulsation observed under the quiet external
77 parameters and within the storm recovery phase at closed and open field lines were from the same source.

78 The present case study is focused on a long-lasting pulsation which took place 08.08.2007 and was recorded
79 simultaneously in the magnetotail and in both polar caps. While ULF fluctuations almost die out in the SW and IMF, ULF
80 activity starts to grow and become more coherent in the magnetosphere as shown from both the Cluster and ground
81 magnetometer data in the both polar caps. To minimize possible influence of both extra-magnetospheric fluctuations and
82 residual activity related to the recovery phase of a geomagnetic storm (Posch et al., 2003) or recent substorm activations, an
83 interval with a quiet conditions both in the interplanetary space and in the magnetosphere have been chosen using the same set
84 of parameters as in (Yagova et al., 2017).

86 **2 Data processing**

87 **2.1 Data**

88 Data from the IMAGE magnetometer network, VOS, DVS, DRV, THL magnetic stations, EISCAT radar, CLUSTER, DMSP
89 as well as OMNI Solar wind and IMF data were utilized. The position of the Cluster satellites and the field line projection of
90 their position (between 12 and 18 UT) together with the location of the stations are given in Figure 1. It should be noted, that
91 the both satellites were in the tail Southern tail lobe for the full day (not shown).

92 IMAGE is a European magnetometer network equipped with three-component flux-gate magnetometers with 10 s initial time
93 resolution (Tanskanen, 2009). The chain is located approximately along the magnetic meridian 100 (MM100), and it covers
94 CGM latitudes from $\Phi=77^\circ$ to 40° . Information on the stations utilised in this study and their coordinates is presented in Table
95 1.

96 The EISCAT Svalbard radar (ESR) is co-located with the LYR magnetometer station ($\Phi=75.4^\circ$) and can make detailed
97 measurements of ionospheric electron density, electron temperature, ion temperature and ion line-of-sight velocity. The radar
98 operates in the 500 MHz band with a peak transmitter power of 1000 kW. In the present paper, data from the 42-meter dish
99 (field aligned pointing position) taken during the International Polar Year (2007–2008) are used.

100 To map the magnetic field variations from the magnetotail to the ground, data from Cluster satellites fluxgate magnetometer
101 have been included (Balogh et al., 1997). The values of footprint coordinates are taken from <https://sscweb.gsfc.nasa.gov/cgi-bin/Locator.cgi>. The Tsyganenko 89C model is used for field line tracing

103 On the 8th of August 2007 (day 220) all four Cluster satellites were located in the southern tail lobe at radial distances of
104 between 15 to 20 R_E . Specifically, fluxgate magnetometer data from Cluster 1 and 3 are used (which had a separation distance
105 of approximately 1 R_E along the Sun-Earth line). Using the TS01 model, Cluster 3 was nearly conjugated with the DRV station
106 (its southern footprint at 17:10 UT was at -68.7° , 141.4° geographic and -76° , 236° CGM).

107 **2.2 Data Processing**

108 Preliminary data processing includes band-pass filtration in the frequency band 0.8-8.3 mHz and decimation to a common
109 1 minute temporal resolution. The lower frequency of the filter window corresponds to ~ 20 min period. An example of spectra
110 of a non-filtered signal can be found in the Figure S1 in the supplementary materials. All spectral maxima at frequencies above
111 1.1 mHz are separated from the filter-related maxima in all the spectra shown as examples and used in statistical analysis.

112 In the case of the magnetospheric satellite measurements of the magnetic field, a local field-aligned system is used. For each
113 time instant, there are two magnetic field vectors in GSE coordinate system, i.e., the instantaneous vector \mathbf{B} and the averaged
114 over the time window one \mathbf{B}_{av} . The field aligned component B_{\parallel} is defined as a projection of \mathbf{B} to \mathbf{B}_{av} . The radial component B_{ρ}
115 is normal to \mathbf{B}_{av} and lies in the plane containing \mathbf{B} and the Earth centre and directed downward. The azimuthal component B_{ϕ}
116 is normal to both B_{\parallel} and B_{ρ} : its direction is determined from the condition that three components form a right-hand triangle.

117 Electron concentration registered by the EISCAT radar are preliminarily sliced with height, averaged, and passed through the
118 low-band filter with a cutoff frequency $f_c=8.3$ mHz. On the day of the case study, 8th August, Svalbard was experiencing the
119 midnight Sun period so the level of background solar radiation incident on the ionosphere was high. Nevertheless, variations
120 of electron density (ΔN_e) are suitable for analysis.
121 The processing of all data (ground and space based) to a common temporal resolution allows a cross-spectral analysis to be
122 performed between the various data sets. The Blackman-Tukey method (Jenkins, 1969; Kay, 1988) is applied to obtain a power
123 spectral density (PSD) for each variable, along with PSD ratio (R), spectral coherence (γ^2) and phase difference ($\Delta\phi$) for each
124 pair of variables. The spectra are calculated in a 96-points (5760 s) sliding window with an 8-min shift between subsequent
125 intervals. Whilst the Blackmann-Tukey method has a more course frequency resolution than other similar methods (such as
126 the Maximum Entropy method), it estimates the PSD with a dispersion which decreases with spectral smoothing.
127 The spectral estimation parameters were chosen as a compromise between two opposite requirements, namely a better
128 frequency resolution and a lower dispersion of the spectral estimation. It should be remembered that the dispersion of spectral
129 coherence and phase difference depends on the absolute value of coherence and goes to zero at $\gamma^2 \rightarrow 1$.
130 OMNI data (time delayed to the Bow Shock) are used for spectral estimations in the IMF whilst Cluster data are used for the
131 magnetotail. Various studies have looked at the response time of the magnetosphere to changes in the Solar Wind (primarily
132 to changes in the IMF). Wing et al. (2002) found a the nightside response time to changes in the IMF of ~12 minutes (at
133 geosynchronous orbit). Given that this study is looking at pulsations with a periodicity of ~12 minutes (1.5 mHz) and using a
134 1.5-hour sampling window for PSD and coherence estimates then the OMNI data has not undergone any additional time lag
135 when evaluating the coherence between that and the Cluster data.

136 3 Results of the analysis

137 3.1 Space weather conditions and ground based magnetometers data on day 220 2007

138 The magnetic field data from the TRO and BZN stations and AE-index, as well as IMF and SW parameters are shown in Figure
139 2, left panel. It is seen from the Figure, that the IMF was undisturbed, and the absolute value of the B_Z component hardly
140 exceed 3 nT. The absolute value of the solar wind speed V was slightly decreasing for the entire period and the mean value
141 was about 500 km/s, which corresponds to moderate SW. The SW dynamic pressure stayed low and there were no rapid
142 changes. The AE index was increasing from 14 UT to 16 UT and there were two enhancements: around 17 UT, and at 20:30
143 UT. **The second enhancement, at 20:30 UT, marked with the vertical blue arrow, corresponds to a substorm.** Although the
144 magnitude of the substorm bay is small (~100 nT), observations by DMSP-satellite (F16, Figure 2b, top right panel) indicate
145 auroral enhancements consistent with a substorm (i.e., particle precipitation occurring from the magnetotail). It should be

146 added that there is no ground based optical observations available in the high latitude northern region due to 24-hour daylight
147 conditions in northern Scandinavia.

148 **3.2 ULF fluctuations on the ground and in space**

149 In this section, the analysis of ULF fluctuations in interplanetary space, the magnetotail and on the ground are presented. The
150 parameters of the IMF/SW fluctuations and geomagnetic pulsations in the magnetotail are calculated throughout the day to
151 illustrate how the parameters of the pulsations in the magnetotail and on the ground are controlled by extra-magnetospheric
152 parameters and the changing (i.e., moving from the auroral oval to the polar cap) of the magnetospheric projection of ground
153 stations. Such a time scale is used in Figures 4(a), 6, 8, and 10. For a more precise analysis of the pulsation spectral properties,
154 a shorter time interval is used in Figures 4(b, c), 11, 12, and 14.

155 **3.2.1 Geomagnetic pulsations on the ground: Northern hemisphere**

156 ULF pulsations are observed in the ground magnetometer data stations located on Svalbard (from NAL to HOR) and at BJR
157 and become indistinct at TRO station, situated on the mainland (Figure 3). For the ground stations, the notations B_N and B_E
158 are used for the components oriented northward along the magnetic meridian, and eastward (orthogonal), respectively. The
159 time series starts at 15:00 UT and stretches for 180 minutes. The maximal amplitude reaches ~ 25 nT peak to peak at $\sim 16:30$ UT
160 for LYR and NAL and then decreases for the value of a few nT.

161 The diurnal variations of the Pi3 (1-4 mHz) power at NAL is controlled by two active regions: the polar cusp, which is
162 responsible for near-noon activity, and the polar boundary of auroral oval in the morning and evening MLT sectors (see Yagova
163 et al. (2004) for details). The station crosses both zones at different UTs with a dependence on seasons and geomagnetic
164 activity in the morning and afternoon MLT sectors. The PSD variation during the day analysed is shown in Figure 4(a). Each
165 data point along the time axis in Figure 4 (b) corresponds to a starting point of a nearly 1.5-hour (96 minute) interval. After
166 the cusp-related maximum near MLT noon (UT=9) (indicated by the vertical red arrow), the PSD reaches a maximum at 13
167 UT (16 MLT) (indicated by the vertical purple arrow). Afternoon Pi3s, seen after 15 UT, do not relate to the cusp activity and
168 are the object of our special interest.

169 To clarify how the contribution of polar cap and auroral oval activity to the NAL pulsations changes with time, the variation
170 of the Pi3 PSD ratio, R , and spectral coherence, γ^2 , for THL-NAL and HOR-NAL station pairs are given on right (Figure 4,
171 b-c). HOR is located ~ 3 degrees southward from NAL on the MM100 chain, while THL lies at $\Phi=84.84^\circ$, i.e., deep in the
172 polar cap. Although THL is shifted by 5.5 hours in MLT from the MM110 stations, the diurnal variation is almost negligible
173 for this location (Yagova et al., 2010) and this station can be taken as an indicator of condition in the polar cap. As it was
174 shown (Yagova et al., 2017), the main pulsation power is concentrated in the frequency band from 1.25 to 1.9 mHz, and UT
175 from 8 to 20, i.e., from pre-noon to almost midnight in MLT. It is seen from the Figure 4b, that both the THL/NAL and
176 HOR/NAL PSD ratio, $R < 1$, at near-noon hours, i.e., NAL is dominating, probably due to cusp-related activity. From 11 to

177 16:30 UT, the THL/NAL spectral ratio, $R > 1$, while HOR/NAL spectral ratio, $R \sim 1$, i.e., the PSD deep in the polar cap is
178 maximal. The HOR/NAL PSD ratio then grows while the THL-NAL PSD ratio remains at ~ 1 . From 13 to 17 UT, the pulsations
179 are coherent for both the THL-NAL and HOR-NAL station pairs with coherence maxima at 14 and 16 UT (Figure 4c). For the
180 first maximum, the HOR-NAL spectral coherence is higher, while for the second one the coherence for the THL-NAL station
181 pair exceeds that for HOR-NAL. This means that after 15 UT, the polar cap (THL) pulsations demonstrate both the highest
182 PSD and coherence with those at NAL. This effect can be associated with NAL moving from the auroral oval to the polar cap
183 or can also result from temporal variations of the pulsation parameters, such as PSD distributions along a meridian and/or
184 spectral coherence.

185 An example of the B_N component variations and their spectral parameters are presented in Figure 5. The left panel (Figure 5a)
186 shows a time series of the B_N component from 15:4417:20 UT from the NAL, THL and HOR stations. The pulsation has a
187 period of approximately 11 minutes (~ 1.5 mHz) and the peak-to-peak amplitude is about 25 nT at NAL and THL, and ~ 15 nT
188 at HOR. Note, that the lower frequency of the filter $f_L=0.8$ mHz corresponds to ~ 20 min period which is almost twice longer
189 than the main pulsation's period. Figures 5b – 5d show the (b) PSD in each location, (c) the interstation spectral coherence,
190 and (d) phase difference. The main maximum of the PSD at all the stations is found at $f_1=1.5$ mHz and the value of the PSD
191 decreases with CGM latitude from THL to HOR (Figure 5b). This spectral coherence for both the NAL-THL and the NAL-
192 HOR station pairs also demonstrate a maximum at $f=f_1$ (as is shown in Figure 5c). Note, that the spectral coherence between
193 NAL and THL (green line in figures 5c and 5d) is higher, than between NAL and HOR (blue line in Figures 5c, d). The
194 pulsations at NAL and THL are almost in phase in the vicinity of f_1 , while a phase difference of $\sim \pi$ exists between NAL and
195 HOR. To summarize, the pulsations in the polar cap are characterised by a clear spectral maximum, and the only difference
196 from typical auroral Pc5s, is a lower frequency of the main maximum ($f_1=1.5$ mHz).

197 3.2.2 Magnetic pulsations in the magnetotail and interplanetary space
198

199 It is commonly believed that the pulsations in the polar caps are directly driven by fluctuations in the SW. To find a source of
200 the studied pulsations, ULF disturbances in the SW, IMF, magnetotail and ionosphere were analysed. The average PSD and
201 coherence of magnetic field fluctuations in the IMF, calculated from OMNI, and in the magnetotail, recorded by Clusters 1
202 and 3, are presented in Figure 6 (over the same frequency range, 1.2–1.9 mHz, as those presented in Figure 4). The variations
203 in PSD of the three IMF components and field aligned component b_{\parallel} in the magnetotail (Cluster3) are given in Figure 6a. One
204 can see from the Figure, that the spectral power in the IMF decreases rapidly at about 13.30 UT (black, dashed arrow in the
205 Figure), and then at ~ 15 UT the decrease is seen in the magnetotail (black solid arrow in figure 6a). Figure 6(b) shows the
206 corresponding PSD in the SW dynamic pressure, P_{SW} , and density, n . Whilst there is an increase in spectral power from
207 10 – 15 UT, there is a sharp decrease at 15 UT, i.e., nearly simultaneously with that of the magnetic field in the magnetotail.

208 Simultaneously, the coherence between the pulsations, as measured by Cluster 3 and Cluster 1, in the magnetotail (Figure 6c)
209 jumps almost to unity, while no severe changes in IMF-Cluster coherence occur. In the coherence panel (figure 6c), only the
210 X-component of IMF is shown as the coherence variations between the Cluster field aligned component, and Y and Z IMF
211 components are similar to the Cluster – IMF b_x coherence. However, the latter demonstrates a closer agreement to the
212 coherence variations within the magnetotail before the pulsation regime changed at about 15 UT (magenta curve in Figure 6c).
213 A similar decrease is found in the coherence between the magnetic field in the magnetotail and P_{sw} , fluctuations (Figure 6d).
214 As the fluctuations of SW density and dynamic pressure were almost identical ($\gamma^2 \sim 1$), only the coherence variations between
215 P_{sw} and Cluster 3 are shown in Figure 6d.
216 The change of pulsation regime in the magnetotail is rather abrupt and it can be seen in the time domain as well. Figure 7
217 shows the pulsations in b_{\parallel} registered simultaneously at Clusters 1 and 3 and their PSD spectra. The time series for the interval
218 started at 15:04 UT is given in Figure 7a. The switch from more or less similar pulsations to almost identical ones is seen at
219 about 15:30 and marked with an arrow. The PSD spectra for the interval started at 15:44 (Figure 7b) has the main spectral
220 maximum at $f=1.5$ mHz, i.e., at the same frequency f_1 , as observed by the ground magnetometers.
221 To quantitatively describe the variation of the spectral shape of the magnetotail pulsations during the day we have used the
222 method described by Yagova et al. (2010, 2015). The technique is based upon an expansion of the function $\sigma(F)$ (a log-log
223 spectrum, where σ and F are the logarithms of PSD and frequency, respectively) into Legendre polynomials with the
224 resulting first 3 coefficients (L_0, L_1, L_2) providing the required quantitative description. In particular, the Q parameter is used
225 (where $Q=-L_2$), which estimates the deviation of the spectrum from an inverse power approximation (colour noise) near the
226 central frequency of interest.
227 The results for the Q -parameter analysis, along with the spectral power ratio and phase difference between the different
228 magnetic field components in the magnetotail, as measured by Cluster 3 are shown in Figure 8. The Q value increases rapidly
229 for all 3 components (b_{\parallel}, b_{ϕ} and b_{ρ}) after the PSD in the IMF decreases (i.e., after the switch off of the mHz fluctuations in the
230 IMF (dash-dot arrow at about 13.30 UT) and it reaches maximal value at 15 UT. It should be noted that at 15 UT, the PSD in
231 the SW pressure decreases rapidly, however, the Q value for the b_{\parallel} and b_{ρ} magnetic field components in the magnetotail
232 remains high ($Q > 0.5$) until 18 UT (and until 17 UT for the b_{ϕ} component). For b_{\parallel} , Q slowly fluctuates between -0.5 and 0.5
233 from 0 at 13 UT and afterwards reaches almost 1 within half an hour. The growth for the transversal components (b_{ϕ} and b_{ρ})
234 after 13:30 UT is not as fast, and Q reaches its maximal value after 15 UT.
235 It has been shown by Pilipenko et al. (2013) that the characteristics of the magnetotail are highly sensitive to the polarization
236 parameters of the pulsations (in comparison to a simple amplitude based investigation). The wave polarisation characteristics
237 were changing during the interval analysed, as seen from the variations of the spectral power ratio, R , and phase difference,
238 $\Delta\phi$, for the $b_{\parallel}b_{\rho}$ and the $b_{\parallel}b_{\phi}$ component pairs (Figures 8b and 8c). For both pairs of components, R exceeds unity almost all
239 day long, i.e., the compressional component is dominating. The only exceptions are registered at 3, 8, and 15 UT. In the
240 afternoon MLT sector, i.e., after 9 UT, it first increases from 2 to nearly 10 and then drops to 2 for the $b_{\parallel}b_{\rho}$ and below unity

241 for the $b_{\parallel}b_{\phi}$ component pairs. Between 1518 UT the average R value is 2-3 times lower than for the previous 3 hours. Averaged
242 over the same frequency band, the sin of the inter-component phase difference, $\Delta\phi$, is shown at the bottom panel. Before 15
243 UT, the parameter varies predominantly in the interval [-0.5, 0.8] and it differs for two component pairs. At 15 UT it changes
244 to almost unity for both component pairs. This corresponds to $\pi/2$ phase difference between field aligned and each of
245 transversal components, indicating a large-scale pulsation with a high fraction of transversal (Alfven) components. The interval
246 of $\pi/2$ phase difference and low R values are seen in Figure 8 from 15 till 18 UT, i.e., it coincides with the interval of low
247 amplitude, high Q and spectral coherence of Pi3 pulsations in the magnetotail.

248 **3.2.3 ULF waves in the magnetotail and on the ground: Inter-hemispheric relationship**

249 Since the Cluster satellites were in the southern tail lobe, only a footprint in the Southern polar region can be calculated. To
250 understand, how the magnetotail pulsations are related to those recorded in the two polar cap ionospheres, the pulsations
251 recorded at Cluster have been compared with those, recorded in the Southern Polar cap, and the latter with the Northern polar
252 cap pulsations. A time series of the pulsations registered simultaneously in the magnetotail at Cluster 3 and in both polar cap
253 ionospheres are presented in Figure 9 (a-c) and the spectral coherence for the pairs of components (1 ground, 1 magnetotail)
254 are given in panels (d-f). Pi3s at the DRV station, which is nominally conjugated with Cluster-3 during this time period, have
255 a peak-to-peak amplitude of about 2 nT (Figure 9a), and the maximal spectral coherence, γ^2 , at 1.5 mHz (f_1) exceeds 0.9 for
256 both field-aligned and transversal components (Figure 9d). It is the maximal value among all the satellite-ground pairs.
257 Pulsations at the VOS station, located deep in the southern polar cap, are similar to the pulsations at Cluster-3 and at DRV.
258 Their peak-to-peak amplitudes reach 4 nT (Figure 9b). The Cluster3-VOS spectral coherence for both components at VOS and
259 the field-aligned component at Cluster-3 is shown in Figure 9e. It reaches a spectral coherence of 0.7 at the frequency, f_1 and
260 is higher than the coherence between the pulsation at VOS and the transversal components at Cluster (not shown here). During
261 this interval, the ground Pi3s are more intensive in the Northern than in the Southern hemisphere. Hence, the peak-to-peak
262 amplitude at NAL is about 25 nT (Figure 9c). The maximal coherence, $\gamma^2 \approx 0.9$, between the NAL and Cluster pulsations is
263 found for the b_{ρ} - b_N component pair (Figure 9f). The results show that there is clearly a high coherence between the pulsations
264 observed in the magnetotail and those in the polar cap ionospheres.

265 A time series of spectral power and coherence, in the 1.2 – 1.9 mHz frequency band, for different pairs of components for
266 Cluster 3 and VOS is presented in Figure 10. The VOS station is taken, because it is located deep within the polar cap at any
267 local time, and thus the influence of the cusp and auroral activity is minimal. A decrease of spectral power at VOS starts
268 immediately after the “switch off” of IMF fluctuations (this instant dash-dot arrow in Figure 10). However, the total decrease
269 of spectral power in the ionosphere is not so severe as in the magnetotail. From 15UT (marked by the black solid arrow) the
270 spectral power measured at VOS remains approximately constant, despite the fact that the spectral power at both Cluster and
271 in the SW dynamic pressure (P_{sw}) (Figure 6b) has decreased significantly. As a result, the tail to ground (T-G) spectral power

272 ratio R_{T-G} during the interval 15-18 UT is high in comparison with the previous hours (Figure 10b). The spectral coherence is
273 also higher than its average value during the day, especially for the b_{\parallel} (Cluster)- b_N (VOS) component pair (Figure 10c).

274 A time series of spectral coherence, in the 1.2 – 1.9 mHz frequency band, between Cluster 3 and 4 ground-based stations in
275 the both hemispheres is shown in Figure 11. The DRV station is nominally conjugated to Cluster-3, the NAL station is located
276 in the Northern hemisphere, VOS and THL are placed deeper in the southern and northern polar caps respectively as it was
277 mentioned above. The three columns of the Figure 11 correspond to the three magnetic field components in the magnetotail,
278 and four rows to the four stations. The two ground horizontal magnetic components are colour coded with b_N in green and b_E
279 in orange. The time interval from 8 to 20 UT corresponds to hours from local noon to midnight at the **TRO station**. The highest
280 coherence is found for the b_N (DRV)- b_{ϕ} (Cluster-3) component pair and last for 2 hours from 15 to 17 UT. During the interval,
281 a large-scale pulsation with a high fraction of transversal (Alfvén) components in the spectral power is recorded in the
282 magnetotail. A high ($\gamma^2=0.7$) but short coherence maximum is seen also in b_N (DRV)- b_{\parallel} (Cluster-3) component pair. A similar
283 to b_N (DRV)- b_{ϕ} (Cluster-3) time evolution is found for the b_E (VOS)- b_{\parallel} (Cluster-3) and b_E (VOS)- b_{ϕ} (Cluster-3) component
284 pairs, but at somewhat lower absolute values of γ^2 . As it is seen from the bottom two rows of panels, during the 15-17 UT time
285 interval, the averaged coherence hardly exceeds 0.5 for all components Cluster 3 - NAL and Cluster 3 - THL, i.e., for stations,
286 located in the Northern polar cap. Generally, the averaged coherence between magnetotail Pi3s with those observed in the
287 northern polar cap is lower than that for the Southern polar cap, as is expected as the Cluster satellites are located in the
288 Southern tail lobe.

289 The inter-relation between the pulsations in the polar caps cannot be completely described by their spectral coherence with the
290 only a single location on open field lines, in the magnetotail. It seems possible to partly compensate for this with the analysis
291 of the coherence between the two polar caps and within each cap. Since the ionospheric observations are available in the
292 Northern hemisphere at the NAL longitude (see table 1), all possible pairs of horizontal components for two combinations of
293 stations (VOS-DVS in the Southern hemisphere, and DVS-NAL between the two hemispheres) were analysed. It should be
294 noted that the maximal coherence at high latitudes is possible not only for the corresponding components (Lepidi et al., 1996).
295 Hence, a maximal coherence can be found for two polar cap stations not between both meridional components, but between
296 e.g., meridional component at the first station and latitudinal component at the second station. The results for the time interval
297 8-20 UT are given in Figure 12. A high coherence ($\gamma^2>0.5$) is seen between the b_N component at VOS and b_E at DVS (Figure
298 12a) and between the b_E component at VOS and both DVS horizontal components for the 15-18 UT interval (Figure 12b).
299 Inter-hemispheric coherence over the same time interval, maximizes for the b_N components of DVS and NAL (Figure 12c).

300 The results of the coherence analysis between the pulsations in the magnetotail and those observed by ground magnetometers
301 in both the Northern and Southern polar caps show that the Pi3 pulsation recorded after 15 UT are characterized by a high
302 coherence both in a space to ground sense and also interhemispherically. A possible interpretation of this is summarized
303 below:

304 1) A compressional/shear Alfvén wave in the magnetotail is propagating predominantly in transversal/field aligned
305 directions, respectively. A high coherence between the pulsations observed by ground magnetometers in each polar
306 cap demonstrate that these waves exist in both tail lobes.

307 2) This leads to coherent pulsations in both polar caps with a higher coherence between the meridional components for
308 nominally conjugated positions and a higher cross-component coherence for the pulsations inside the Southern polar
309 cap.

310 **3.2.4 Electron density fluctuations in the ionosphere**

311 To examine electron density fluctuations in the ionosphere over different altitudes EISCAT radar data have been used. The
312 background Ne level was high due to Solar Extreme Ultraviolet (EUV) ionisation but the application of a low-bound filter (see
313 sect. 2.2) allows fluctuations of electron density ΔN_e for each altitude to be calculated.

314 A time series of ΔN_e , centred in the F-region (at $h=205$ km) along with the b_N component of magnetic field at NAL is shown
315 in Figure 13a. The spectral power of both time series is shown in figure 13b, their spectral coherence in figure 13c and the
316 phase difference in figure 13d. The analysis indicates a common spectral maximum at $f_i=1.5$ mHz (Figure 13b) with a wide
317 coherence maximum with $\gamma_{\max} \approx 0.9$ (Figure 13c). The pulsations are in anti-phase with one another, as is clearly seen from
318 both the time series and the phase-difference, which is nearly π at the f_i frequency (Figure 13d).

319 Figure 14(a) shows the temporal variation of the spectral coherence, γ^2 (in the frequency band 1.2–1.9 mHz) between ΔN_e and
320 the b_N component of the magnetic field over an altitude range covering the E and F-regions of the ionosphere (from 100 –
321 450 km). Before 16:30 UT, the highest spectral coherence is registered with maximum at about 200 km. The same altitude of
322 maximal coherence is seen from 16:40 until 17:30 UT. Several spots of high coherence were found at lower (~150 km centred
323 at 17 UT) and higher (350 km around 16:30 UT and 420 km at 17-17:30 UT) altitudes. An altitude profile taken at 15:44 UT
324 is shown in Figure 14b. Spectral coherence is high ($\gamma^2 > 0.5$) in the altitude range from 120 to 350 km, and the maximal
325 coherence is found at $h = 205$ km. This high coherence between the geomagnetic and N_e pulsations can be a result of modulated
326 particle precipitation. The altitudes where the highest coherence is found, correspond to the penetration altitude of electrons
327 with energies in the hundreds of eV.

328 **4 Discussion**

329 **Highly coherent pulsations in the Pc5/Pi3 range were observed in the magnetotail and inside the polar caps on the 8th August
330 2007.** A spectral analysis of the IMF and SW parameters indicated that the amplitude of pulsations of a similar frequency had
331 decreased significantly by 13:30 and 15:00 UT respectively (Figure 6). Observations made in the magnetotail (by the Cluster
332 satellites) and in the polar caps (by ground magnetometers and the EISCAT radar) indicate that, at the same time (15 UT), the

333 Pc5/Pi3 ULF characteristics in this region changed. A most impressive feature of the pulsations in the magnetotail **during the**
334 **studied hours is** a high Q factor, with a central frequency about 1.5 mHz and extremely high coherence between the two Cluster
335 satellites. The visible pulsations are almost in-phase. At the same moment the contribution of b_p and b_ϕ (transverse) components
336 to the total spectral power increases. The pulsations are also recorded in both polar caps by ground magnetometers. A
337 coherence analysis shows that the maximal coherence is found for nominally conjugated positions in the magnetotail and in
338 the southern polar cap ionosphere and between the two hemispheres for the transversal magnetic field components in the
339 magnetotail and the b_N in the ground magnetometer data. For non-conjugated position in the same hemisphere the coherence
340 is higher for the field-aligned component in the magnetotail and b_E in the ground magnetometer data. This could mean that the
341 wave is a combination of a compressional mode and shear Alfvén modes contributing predominantly to wave transport in
342 transversal and parallel direction to **B**, respectively. The pulsations also show a high coherence between variations of electron
343 concentration, ΔN_e , and the ground magnetic b_N component in the northern polar cap ionosphere. The fact that it is registered
344 in the electron concentration could indicate modulated particle precipitation into the ionosphere from the magnetotail.

345 These high quality Pc-like pulsations in the magnetotail probably correspond to some resonance magnetotail mode and started
346 after the external fluctuations had been switched off. Thus, one can speculate that usually the pulsations in the magnetotail are
347 masked by a higher amplitude broadband ULF “noise” of extra-magnetospheric origin. The existence of quasi-resonance
348 modes at open field lines has been discussed by previous authors, for different types of pulsations. Physically they are related
349 to the reflection of inhomogeneities in the distribution of the Alfvén velocity (e.g., Pilipenko et al., 2005). Also, as discussed
350 by (Leonovich, and Kozlov, 2018) the laterally inhomogeneous structure of the nightside magnetosphere can also result in
351 various resonance and waveguide MHD modes in the Pc3-6 frequency range.

352 It is interesting to note, that the studied event perfectly matches with the dataset used in (Yagova et al, 2017), where the authors
353 show, that that the parameter Q is higher for pre-substorm pulsations, than for the typical polar cap Pi3s. However, given the
354 current dataset it is not possible to conclusively link this ULF wave event to the substorm observed at 20.30UT.

355

356 5. Conclusion

- 357 • Geomagnetic pulsations with a frequency $f_l \sim 1.5$ mHz were registered on open field lines, in both the Northern and
358 Southern polar caps during quiet, static, space weather conditions on the 8th August 2007.
- 359 • These pulsations were also observed in the magnetotail with remarkably high quality and coherence both in space
360 and between the magnetotail and polar cap in Earth.
- 361 • The pulsations are seen simultaneously in the ionospheric electron density enhancements in the Northern Polar Cap.

362 ● The maximal coherence is found for nominally conjugated positions in the magnetotail and in the southern polar cap
363 ionosphere; and between the two hemispheres for the transversal magnetic field components in the magnetotail and
364 the meridional (b_N) component in the ground magnetometer data.

365 ● For non-conjugated positions in the same hemisphere the coherence is higher for the field-aligned component in the
366 magnetotail and latitudinal (b_E) component in the ground magnetometer data.

367 ● This indicates that the wave is a combination of a compressional mode and shear Alfvén modes contributing
368 predominantly to wave transport in the transversal and parallel direction to \mathbf{B} , respectively.

369

370

371 **Data availability:** Publicly available ground-based magnetometer data: IMAGE through <https://space.fmi.fi/image/www/>,
372 INTERMAGNET through www.intermagnet.org. Magnetometer data from VOS station are available through
373 (<http://geophys.aari.ru>) upon request. EISCAT data are publicly available through <https://www.eiscat.se/scientist/data/>. Cluster
374 and OMNI data are publicly available through CDAWEB (<https://cdaweb.gsfc.nasa.gov>). The maps in Figure 1 are made with
375 Natural Earth (Free vector and raster map data <https://www.naturalearthdata.com>).

376 **Author contribution:** NN suggested the event for the case-study, prepared ground-based data for preliminary analysis. NY
377 developed software and performed data analysis. LB assisted with EISCAT data analysis and DL assisted with DMSP data
378 analysis. DS provided Vostok data. The manuscript was prepared by NN and NY, after discussions with LB and DL.

379 **Acknowledgements:** The authors thank prof. V.A. Pilipenko for helpful discussions. The authors thank the institutes who
380 maintain the IMAGE Magnetometer Array: Tromsø Geophysical Observatory of UiT the Arctic University of Norway
381 (Norway), Finnish Meteorological Institute (Finland), Institute of Geophysics Polish Academy of Sciences (Poland), GFZ
382 German Research Centre for Geosciences (Germany), Geological Survey of Sweden (Sweden), Swedish Institute of Space
383 Physics (Sweden), Sodankylä Geophysical Observatory of the University of Oulu (Finland), and Polar Geophysical Institute
384 (Russia). The results presented in this paper rely on data collected at magnetic observatories. The authors thank the national
385 institutes that support them and INTERMAGNET for promoting high standards of magnetic observatory practice
386 (www.intermagnet.org). The authors thank the Arctic and Antarctic Research Institute in Russia for providing ground
387 magnetometer data from VOS station (<http://geophys.aari.ru>). The authors thank CDAWEB (<https://cdaweb.gsfc.nasa.gov>) for
388 Cluster and OMNI data. EISCAT is an international association supported by research organisations in China (CIRIP),
389 Finland (SA), Japan (NIPR and ISEE), Norway (NFR), Sweden (VR), and the United Kingdom (UKRI). This research was
390 partly funded by the PolarProg and INTPART research programs under the Research Council of Norway (project numbers
391 246725 and 309135, NN, LB, DL) and by RFBR grant # 20-05-00787 A (NY).

392 The authors declare that they have no conflict of interest.

393 **References**

394 Allan, W., and Wright, A. N.: Magnetotail waveguide: Fast and Alfvén waves in the plasma sheet boundary layer and lobe, *J. Geophys. Res.*, 105(A1), 317–328, doi:[10.1029/1999JA900425](https://doi.org/10.1029/1999JA900425), 2000.

395 Alperovich, L. S. and Fedorov, E. N.: Hydromagnetic Waves in the Magnetosphere and the Ionosphere, Series: Astrophysics
396 and Space Science Library, vol. 353, 2009, XXIV, 418p., Hardcover, ISBN: 978-1-4020-6636-8, 2007.

397 Baker, G., Donovan, E. F., Jackel, B. J.: A comprehensive survey of auroral latitude Pc5 pulsation characteristics. *Journ. Geophys. Res. Space Phys.*, 108, 1384, 2003.

398 Ballatore, P.: Pc5 micropulsation power at conjugate high-latitude locations, *J. Geophys. Res.*, 108, 1146,
399 doi:[10.1029/2002JA009600](https://doi.org/10.1029/2002JA009600), 2003.

400 Balogh, A., Dunlop, M. W., Cowley, S. W. H., Southwood, D. J., Thomlinson, J. G., Glassmeier, K. H., Musmann, G., Luhr,
401 H., Buchert, S., Acuna, M. H., Fairfield, D. H., Slavin, J. A., Riedler, W., Schwingenschuh K., and Kivelson, M. G.: The
402 Cluster Magnetic Field Investigation. *Space Sci. Rev.*, 79, 65–91, doi:[10.1023/A:1004970907748](https://doi.org/10.1023/A:1004970907748), 1997

403 Bland, E. C., and McDonald, A. J.: High spatial resolution radar observations of ultralow frequency waves in the southern
404 polar cap, *J. Geophys. Res. Space Physics*, 121, 4005–4016, doi:[10.1002/2015JA022235](https://doi.org/10.1002/2015JA022235), 2016.

405 Bolshakova, O.V. and Troitskaya, V.A.: Dayside cusp dynamics from the observations of long-period geomagnetic
406 pulsations, *Geomagn. Aeron.*, 17, 1076–1082, 1977.

407 Borovsky, J. E., and Denton, M. H.: Exploring the cross correlations and autocorrelations of the ULF indices and incorporating
408 the ULF indices into the systems science of the solar wind-driven magnetosphere, *Journ. Geophys. Res. Space Physics*, 119, 4307–4334, doi:[10.1002/2014JA019876](https://doi.org/10.1002/2014JA019876), 2014.

409 De Lauretis, M., Regi, M., Francia, P., Marcucci, M. F., Amata, E., and Pallocchia, G.: Solar wind-driven Pc5 waves observed
410 at a polar cap station and in the near cusp ionosphere, *Journ. Geophys. Res. Space Phys.*, 121, 11,145–11,156,
411 doi:[10.1002/2016JA023477](https://doi.org/10.1002/2016JA023477), 2016.

412 Francia, P., Lanzerotti, L. J., Villante, U., Lepidi, S., and Di Memmo, D.: A statistical analysis of low-frequency magnetic
413 pulsations at cusp and cap latitudes in Antarctica, *J. Geophys. Res.*, 110, A02205, doi:[10.1029/2004JA010680](https://doi.org/10.1029/2004JA010680), 2005.

414 Han, D.-S., Yang, H.-G., Chen, Z.-T., Araki, T., Dunlop, M. W., Nosé, M., Iyemori, T., Li, Q., Gao, Y.-F., and Yumoto,
415 K.: Coupling of perturbations in the solar wind density to global Pi3 pulsations: A case study, *Journ. Geophys. Res.*, 112,
416 A05217, doi:[10.1029/2006JA011675](https://doi.org/10.1029/2006JA011675), 2007.

417 Heacock, R., and Chao, J.: Type Pi Magnetic field pulsations at very high latitudes and their relation to plasma
418 convection in the magnetosphere, *J. Geophys. Res.*, 85(A3), 1203–1213, doi:[10.1029/JA085iA03p01203](https://doi.org/10.1029/JA085iA03p01203), 1980.

419 Keiling, A., Alfvén Waves and Their Roles in the Dynamics of the Earth's Magnetotail: A Review, *Space Sci Rev*, 142: 73–
420 156, doi:[10.1007/s11214-008-9463-8](https://doi.org/10.1007/s11214-008-9463-8), 2009.

421 Kepko, L., Spence, H. E., and Singer, H. J.: ULF waves in the solar wind as direct drivers of magnetospheric pulsations,
422 *Geophys. Res. Lett.*, 29, 1197, doi:[10.1029/2001GL014405](https://doi.org/10.1029/2001GL014405), 2002.

426 Kepko, L., Viall, N. M., and Wolfinger, K.: Inherent length scales of periodic mesoscale density structures in the solar wind
427 over two solar cycles. *Journal of Geophysical Research: Space Physics*, 125, e2020JA028037.
428 <https://doi.org/10.1029/2020JA028037>, 2020.

429 Kozyreva, O., Pilipenko, V., Engebretson, M. J., Yumoto, K., Watermann, J., and Romanova, N.: In search of a new ULF
430 wave index: Comparison of Pc5 power with dynamics of geostationary relativistic electrons, *Planet. Space Sci.*, **55**, 755, 2007.

431 Leonovich, A. S., and Kozlov, D. A.: Kelvin-Helmholtz instability in the geotail low-latitude boundary layer. *Journal Geophys.*
432 *Res.: Space Phys.*, 123, 6548– 6561. <https://doi.org/10.1029/2018JA025552>, 2018.

433 Lepidi, S., Villante, U., Vellante, M., Palangio, P., and Meloni, A.: High resolution geomagnetic field observations at Terra
434 Nova Bay, Antarctica, *Ann. Geophys.*, 39, 519– 528, doi:10.4401/ag-3987, 1996.

435 Lyons, L. R., Nagai, T., Blanchard, G. T., Samson, J. C., Yamamoto, T., Mukai, T., Nishida, A., and Kokubun,
436 S.: Association between Geotail plasma flows and auroral poleward boundary intensifications observed by CANOPUS
437 photometers, *J. Geophys. Res.*, 104 (A3), 4485– 4500, doi:[10.1029/1998JA900140](https://doi.org/10.1029/1998JA900140), 1999.

438 Lyons, L. R., Nishimura, Y., Kim, H.-J., Donovan, E., Angelopoulos, V., Sofko, G., Nicolls, M., Heinselman,
439 C., Ruohoniemi, J. M. , and Nishitani, N.: Possible connection of polar cap flows to pre- and post-substorm onset PBIs and
440 streamers, *J. Geophys. Res.*, 116, A12225, doi:10.1029/2011JA016850, 2011.

441 Mann, I.R., Voronkov, I., Dunlop M., et al., Coordinated ground-based and Cluster observations of large amplitude global
442 magnetospheric oscillations during a fast solar wind interval. *Ann. Geophys.* 20, 405–426, 2002

443 Nishimura, Y., Lyons, L. R., Shiokawa, K., Angelopoulos, V. Donovan, E. F., and Mende , S. B.: Substorm onset and
444 expansion phase intensification precursors seen in polar cap patches and arcs, *J. Geophys. Res. Space Physics*, 118, 2034–
445 2042, doi:10.1002/jgra.50279, 2013.

446 Nishimura, Y., et al.: Coordinated ionospheric observations indicating coupling between preonset flow bursts and waves that
447 lead to substorm onset, *J. Geophys. Res. Space Physics*, 119, 3333– 3344, doi:[10.1002/2014JA019773](https://doi.org/10.1002/2014JA019773), 2014.

448 Pilipenko, V. A., N. G. Mazur, E. N. Federov, M. J. Engebretson, and D. L. Murr, Alfvén wave reflection in a curvilinear
449 magnetic field and formation of Alfvénic resonators on open field lines, *J. Geophys. Res.*, 110, A10S05,
450 doi:10.1029/2004JA010755, 2005.

451 Pilipenko, V.A., Kawano, H., and Mann, I.R.: Hodograph method to estimate the latitudinal profile of the field-line resonance
452 frequency using the data from two ground magnetometers. *Earth Planet Sp* 65, 5, doi:10.5047/eps.2013.02.007, 2013.

453 Posch, J. L., Engebretson, M. J., Pilipenko, V. A., Hughes, W. J., Russell, C. T., and Lanzerotti, L. J.: Characterizing the long-
454 period ULF response to magnetic storms, *J. Geophys. Res.*, 108, 1029, doi:10.1029/2002JA009386, A1, 2003.

455 Rae, I.J., Donovan, E. F., Mann, I. R., Fenrich, F. R., Watt, C. E. J., Milling, D. K., Lester, M., Lavraud, B., Wild, J. A., Singer,
456 H. J., Rème, H., Balogh, A., Evolution and characteristics of global Pc5 ULF waves during a high solar wind speed interval.
457 *J. Geophys. Res.* 110, A1221, doi:10.1029/2005JA011007, 2005.

458 Shi, X., Baker, J. B. H., Ruohoniemi, J. M., Hartinger, M. D., Murphy, K. R., Rodriguez, J. V., et al. Long-lasting poloidal
 459 ULF waves observed by multiple satellites and high-latitude SuperDARN radars. *Journal of Geophysical Research: Space Physics*, 123, 8422–8438. <https://doi.org/10.1029/2018JA026003>, 2018

460

461 Shi, X., Hartinger, M. D., Baker, J. B. H., Ruohoniemi, J. M., Lin, D., Xu, Z., et al.: Multipoint conjugate observations of
 462 dayside ULF waves during an extended period of radial IMF. *Journal of Geophysical Research: Space Physics*, 125,
 463 e2020JA028364. <https://doi.org/10.1029/2020JA028364>, 2020.

464 Wang, G. Q., Zhang, T. L., and Volwerk, M.: Statistical study on ultralow-frequency waves in the magnetotail lobe observed
 465 by Cluster, *J. Geophys. Res. Space Physics*, 121, 5319–5332, doi:10.1002/2016JA022533, 2016.

466 Weatherwax, A. T., Rosenberg, T. J., Maclennan, C. G. Doolittle, J. H. : Substorm precipitation in the polar cap and associated
 467 Pc 5 modulation, *Geophys. Res. Lett*, 24, 579-582, 1997.

468 Wing, S., Sibeck, D. G., Wiltberger, M., and Singer, H.: Geosynchronous magnetic field temporal response to solar wind and
 469 IMF variations, *J. Geophys. Res.*, 107(A8), 1–10, doi:10.1029/2001JA009156, 2002.

470 Yagova, N., Pilipenko, V., Rodger, A., Papitashvili, V., and Watermann, J.: Long period ULF activity at the polar cap
 471 preceding substorm, in: Proc. 5th International Conference on Substorms, St. Peterburg, Russia (ESA SP-443), 603–606, 2000.

472 Yagova, N. V., Pilipenko, V. A., Lanzerotti, L. J., Engebretson, M. J., Rodger, A. S., Lepidi, S., and Papitashvili, V. O., Two-
 473 dimensional structure of long-period pulsations at polar latitudes in Antarctica, *J. Geophys. Res.*, 109, A03222,
 474 doi:10.1029/2003JA010166, 2004

475 Yagova N., Pilipenko, V., Watermann, J., Yumoto, K.: Control of high latitude geomagnetic fluctuations by interplanetary
 476 parameters: The role of suprathermal ions, *Annales Geophysicae*, 25, 1037-1047, 2007.

477 Yagova, N. V., Spectral Slope of High-Latitude Geomagnetic Disturbances in the Frequency Range 1–5 mHz. Control
 478 Parameters Inside and Outside the Magnetosphere, *Geomagn. Aeron.*, 55, 32-40, 2015

479 Yagova, N., Nosikova, N., Baddeley, L., Kozyreva, O., Lorentzen, D. A., Pilipenko, V., and Johnsen, M. G.: Non-triggered
 480 auroral substorms and long-period (1–4 mHz) geomagnetic and auroral luminosity pulsations in the polar cap, *Ann. Geophys.*,
 481 35, 365–376, doi:10.5194/angeo-35-365-2017, 2017.

482 Zhang, S., Tian, A., Shi, Q., Li, H., Degeling, A. W., Rae, I. J., Forsyth, C., Wang, M., Shen, X., Sun, W., Bai, S., Guo, R.,
 483 Wang, H., Fazakerley, A., Fu, S., and Pu, Z.: Statistical study of ULF waves in the magnetotail by THEMIS observations,
 484 *Ann. Geophys.*, 36, 1335–1346, <https://doi.org/10.5194/angeo-36-1335-2018>, 2018.

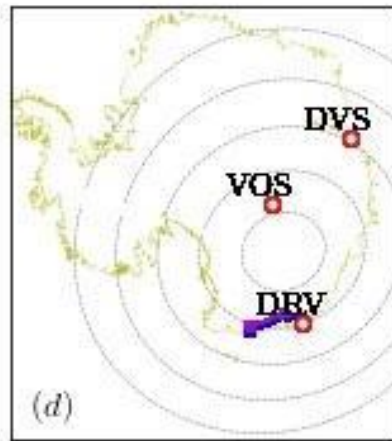
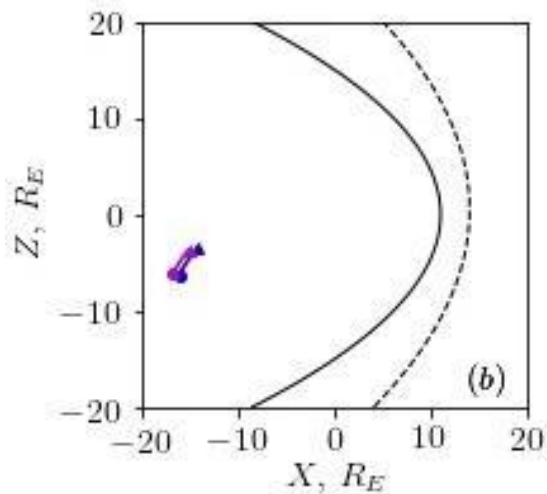
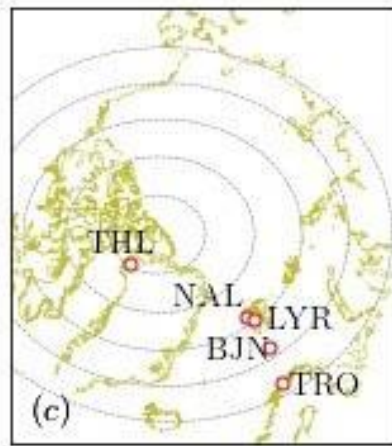
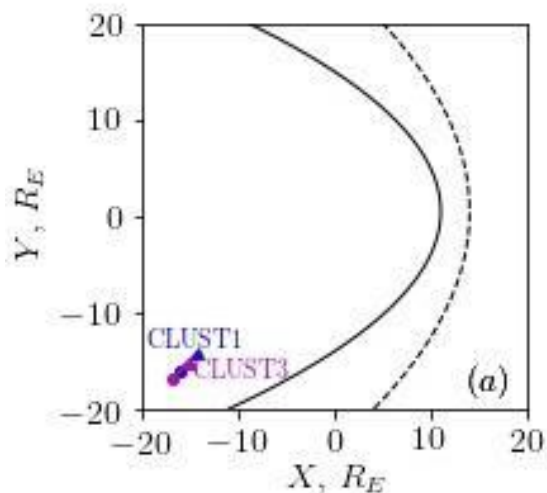
485

486 Table 1. Station coordinates and their parameters

Station code	Geographic		Geomagnetic (CGM)		UT of MLT midnight
	Latitude	Longitude	Latitude	Longitude	
NAL	78.92	11.95	76.34	110.45	20:59

LYR	78.20	15.82	75.40	111.20	20:55
HOP	76.5	25.1	73.22	114.53	20:40
TRO	69.66	18.95	66.75	102.42	21:26
THL	77.48	290.83	84.84	29.19	3:13
DRV	-66.66	140.01	-80.37	236.04	12:55
VOS	-78.46	106.82	-83.57	55.15	1:02
DVS	-68.58	77.97	-74.75	101.17	21:58

487
488
489
490
491
492



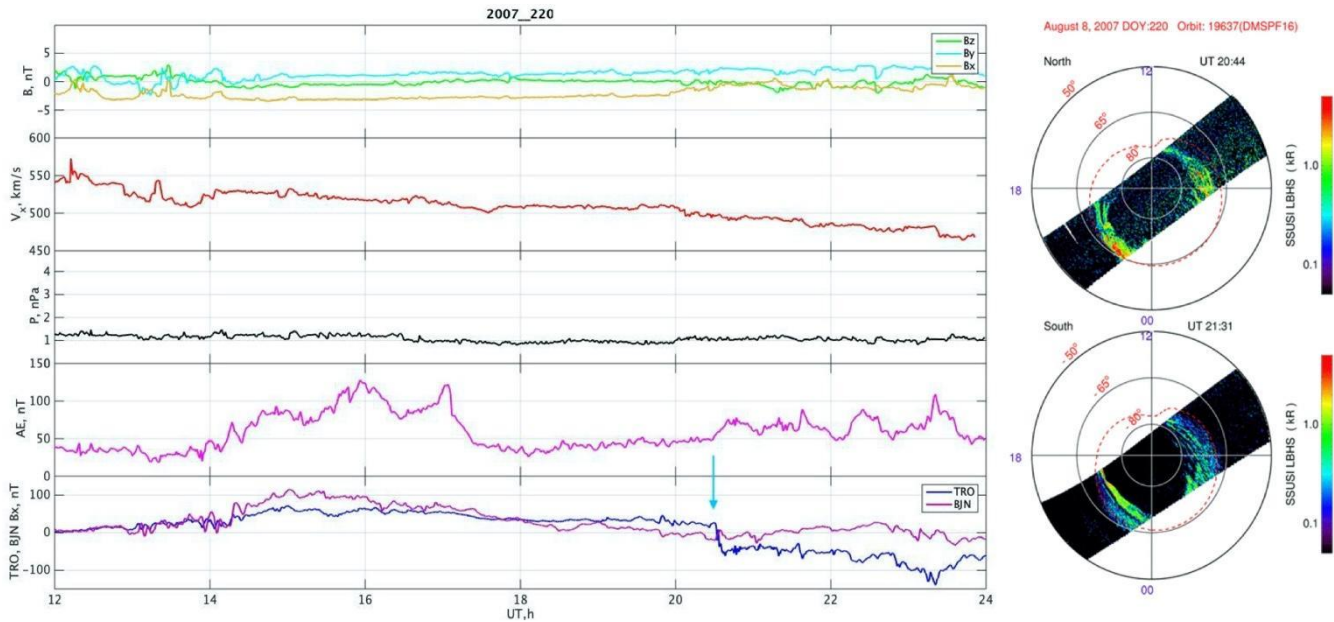
493

494

495

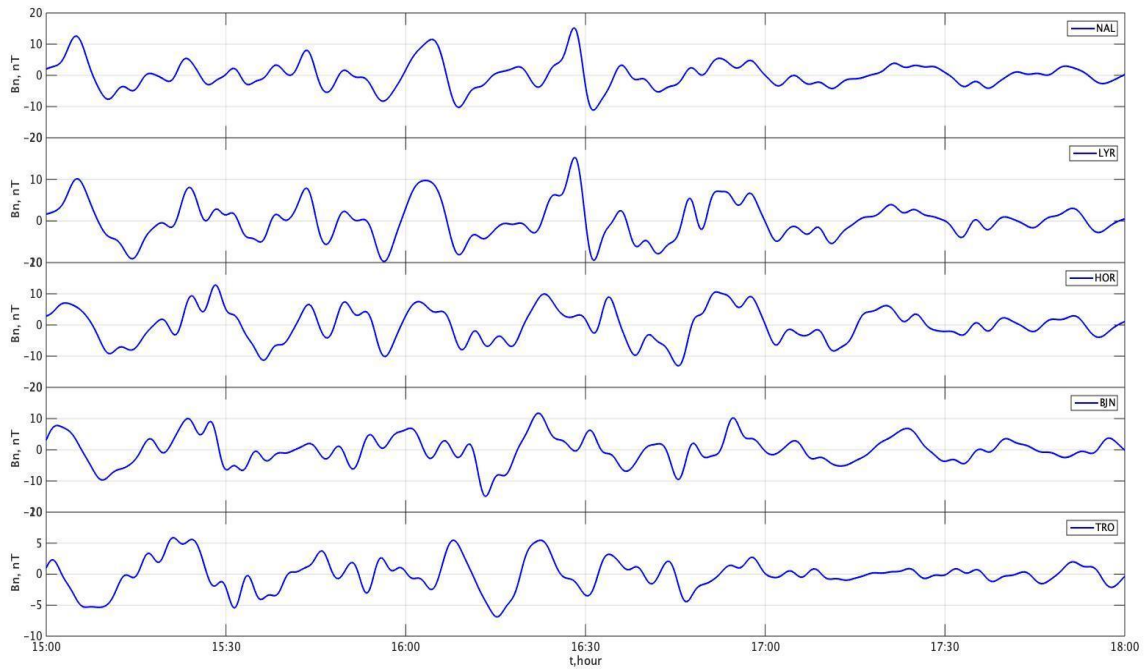
496

Figure 1: Cluster 1 and 3 satellites orbits in GSE coordinates (XY – panel (a), XZ –(b)) and their projection on the map with observatories located in the (c) Northern and (d) Southern hemispheres (12-18 UT). The initial point and final point are marked with a circle and a triangle, respectively.



497
498
499
500

Figure 2: The particle precipitation seen from the DMSP satellite (right panel) and the solar wind parameters as well as ground based magnetometers data (left panel, from top to bottom: IMF all components; SW speed; SW pressure; AE-index; the magnetic field data from the TRO and BZN stations. A small substorm is marked with the vertical blue arrow).

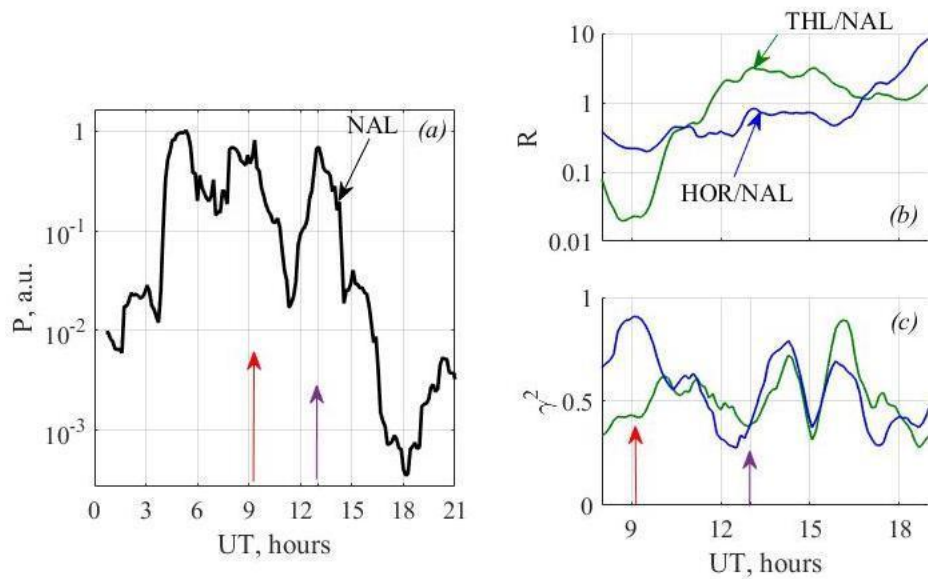


501

502

Figure 3: A latitude profile of geomagnetic pulsations registered on Svalbard (4 top panels) and at Tromsø (the bottom panel).

503

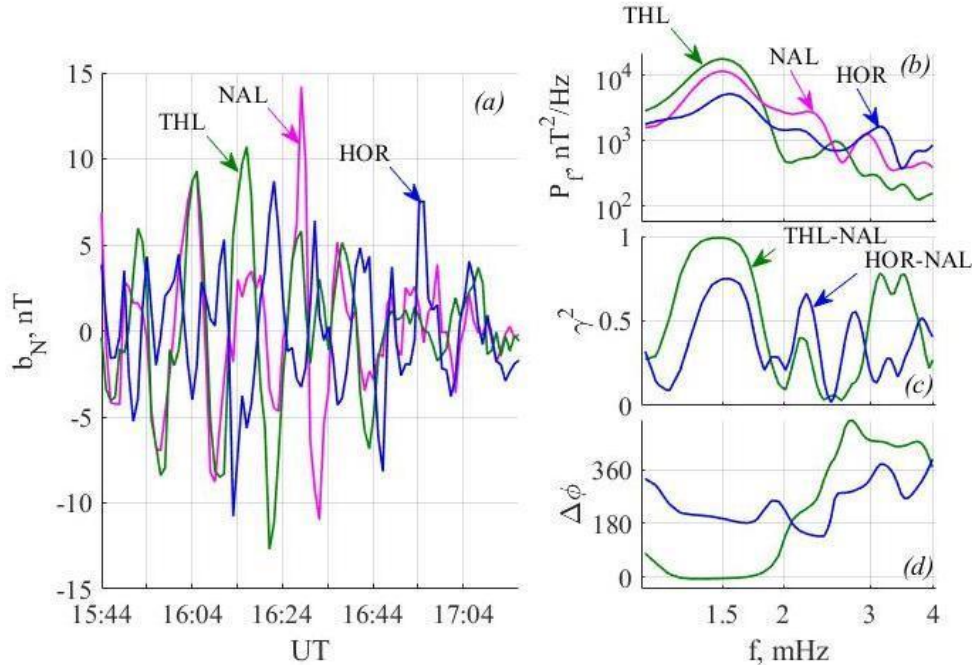


504

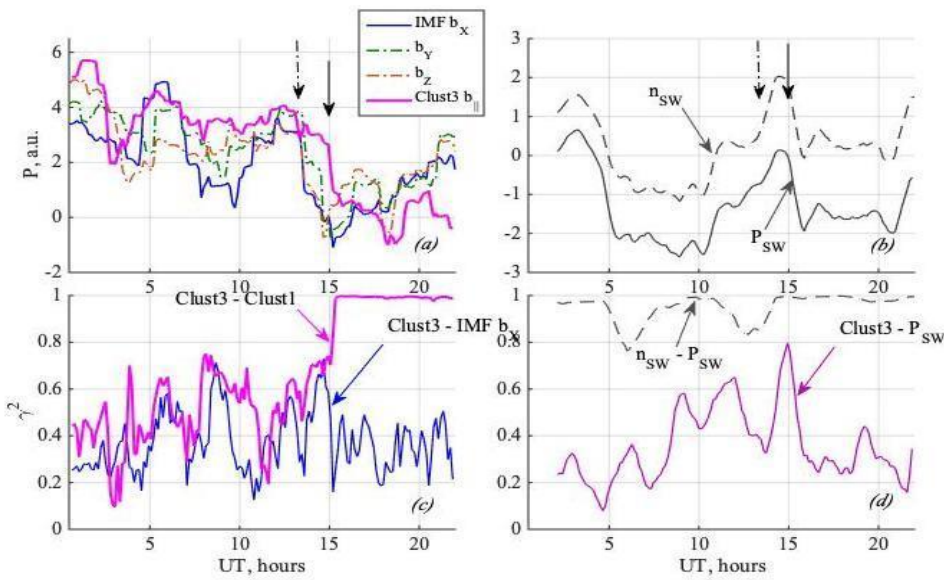
Figure 4: (a) Diurnal variations of the spectral power in 1.2-1.9 mHz frequency band for NAL b_N component (b) PSD spectral ratio and (c), spectral coherence for the NAL-THL and NAL-HOR station pairs. Near-noon and afternoon maxima are marked by arrows.

505

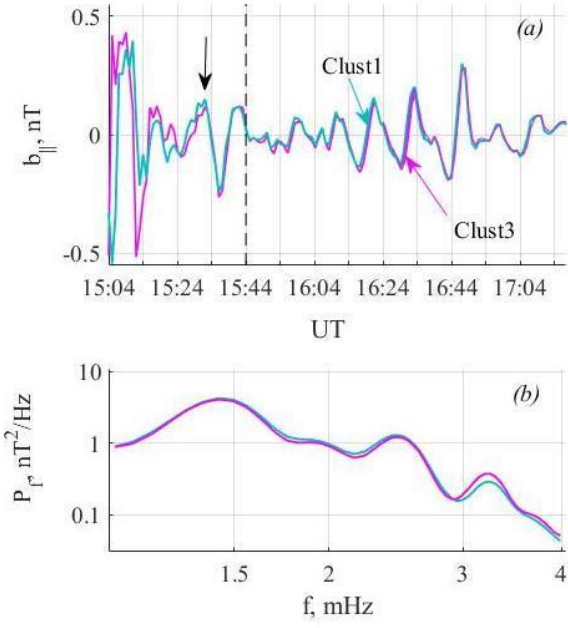
506



508 **Figure 5:** (a) Pulsations of b_N component at NAL, THL, and HOR during the interval starting at 15:44 UT; (b) PSD spectra; (c)
 509 spectral coherence for THL- NAL and HOR- NAL pairs of stations; (d) phase differences. THL- NAL and HOR- NAL station pairs
 510 at panels (c) and (d) are shown with the same colours as THL and HOR at panels (a) and (b).

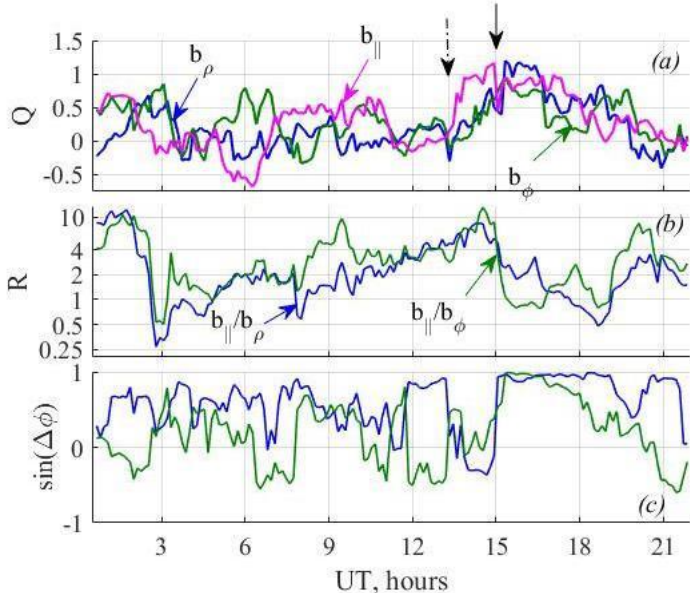


512 **Figure 6:** Left column: Time variations of (a) spectral power and (c) average spectral coherence for the three IMF components
 513 (GSM) and field aligned b_{\parallel} components at Clusters 1 and 3. Right column: (b) variations of total spectral power and (d) average
 514 spectral coherence for the SW density and SW dynamic pressure as well as field aligned b_{\parallel} components at Clusters 3. The dot-dash
 515 and solid arrows indicate the time at which there is a significant decrease of the spectral power in the IMF fluctuations (dot-dashed),
 516 and in b_{\parallel} at Cluster and the SW density and pressure (solid).



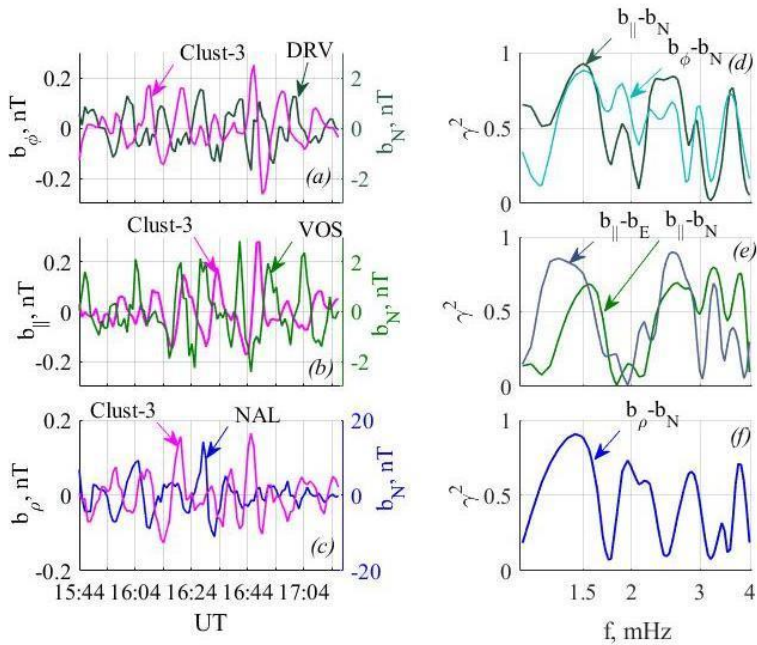
517

518 **Figure 7:** (a) Pulsations of b_{\parallel} component in the magnetotail, recorded by Clusters 1 and 3 during the interval starting at 15:04 UT;
 519 and (b) PSD spectra for the 96-min interval starting at 15:44 (the start instant of the window, for which the spectra are calculated
 520 is marked with a vertical dashed line). The change of pulsation regime is marked with an arrow. Pulsations at Clusters 1 and 3 are
 521 shown with the same colours in all the panels



522

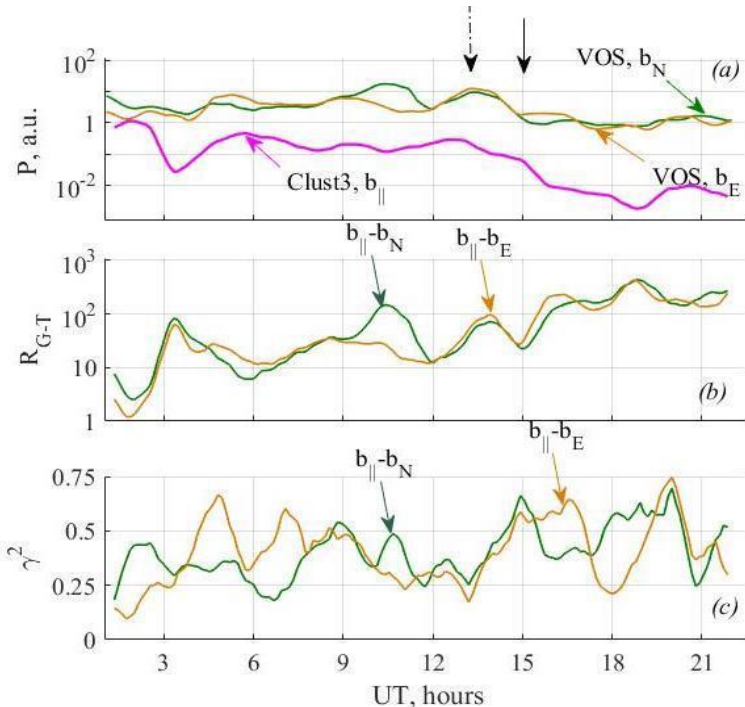
523 **Figure 8: Time variations of (a) the parameter Q , (b) spectral field-aligned to transversal components spectral power ratio R , and**
 524 **(c) the sinus of phase difference at Cluster 3. The change of pulsation regime in the IMF (at 13:30UT) and in b_{\parallel} at Cluster at 15 UT**
 525 **is marked by the arrows, similar to Figures 7.**



526

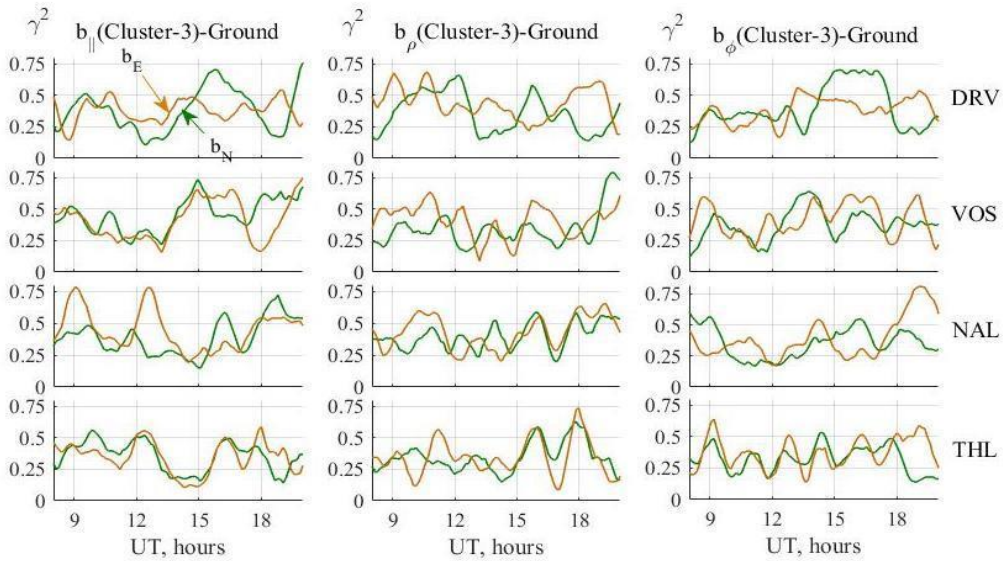
527
528
529
530

Figure 9: Pulsations in the magnetotail (Cluster-3) and of b_N on Earth. Pulsations at Cluster 3 and one of the ground stations are shown in panels (a-c). A component with the maximal coherence at the f_1 frequency with the corresponding station is shown at each of a-c panels. Left/right Y-axis correspond to Cluster 3/ground, respectively. Spectral coherence for the same satellite –station pairs are given in panels (d-f).



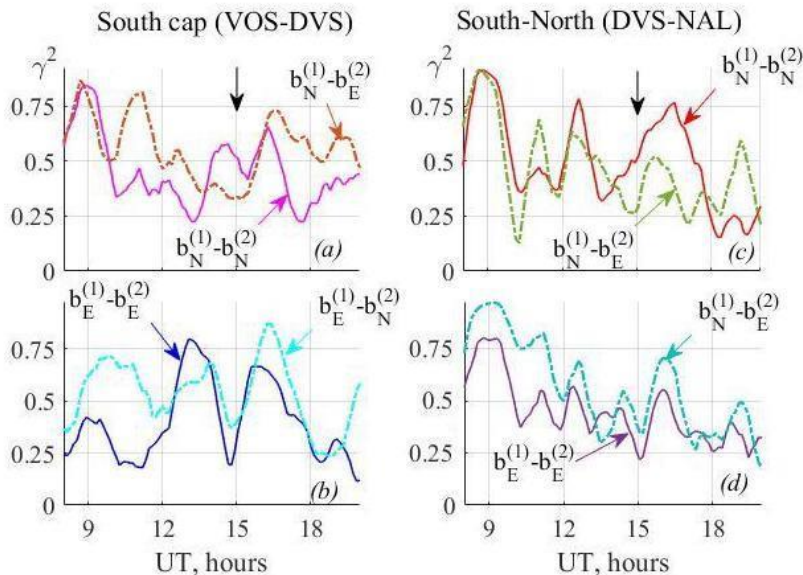
531

Figure 10: Time variations of (a) spectral power, (b) ground to tail spectral ratio R_{G-T} , and average (c) spectral coherence in the 1.2–1.9 mHz frequency band for b_{\parallel} components at Cluster 3 and both horizontal components at VOS. Time instants of decrease of spectral power of IMF fluctuations and pulsations in b_{\parallel} at Cluster are marked with dot-dash and solid arrows, respectively.



535

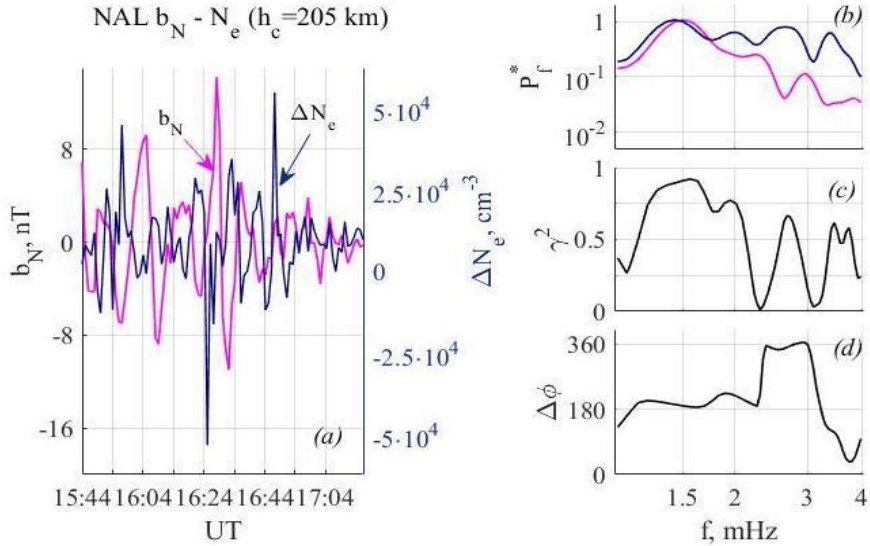
536 **Figure 11:** Time variations of average spectral coherence in 1.2-1.9 mHz frequency band for all component pairs formed from
 537 Cluster-3 and the 4 stations. 3 columns correspond to $b_{||}$, b_{ρ} , and b_{ϕ} Cluster components, and the rows show the DRV, VOS, NAL,
 538 and THL stations. The b_N and b_E components on Earth are shown in green and orange, respectively.



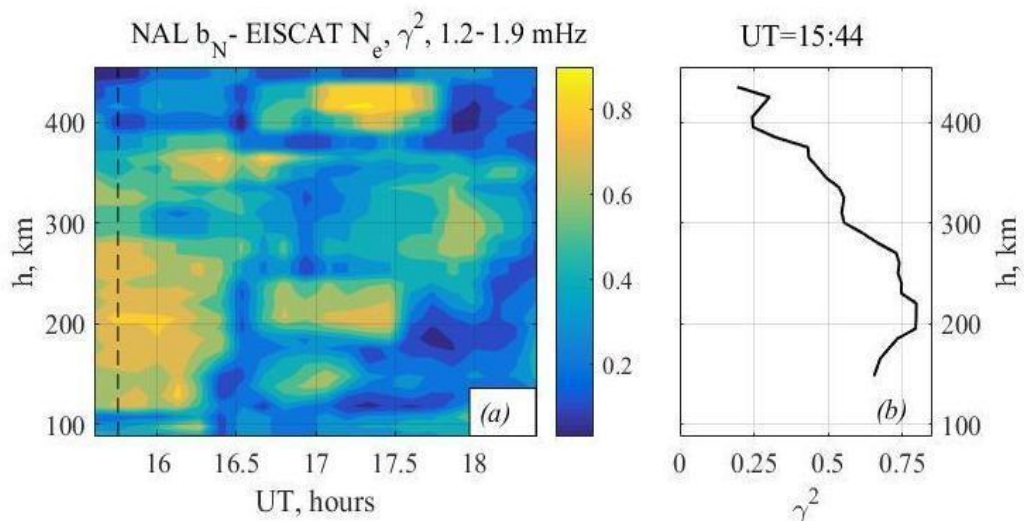
539

540 **Figure 12:** Time variations of average spectral coherence in 1.2-1.9 mHz frequency band between two points in the Southern polar
 541 cap and between the Southern and the Northern polar cap stations: (a) b_N component at VOS - both horizontal components at DVS;

542 (b) b_E component at VOS - both horizontal components at DVS; (c) b_N component at DVS - both horizontal components at NAL; (d)
 543 b_E component at DVS - both horizontal components at NAL. Coherence for corresponding components (NN and EE) is shown in all
 544 the panels with solid lines, and cross-component (NE and EN) coherence is shown with dash-dot lines. Upper indexes indicate the
 545 number of a station in the station pair. The time at which there is a decrease in the spectral power of the pulsations at Cluster are
 546 marked with an arrow.



547
 548 **Figure 13:** (a) Pulsations of b_N component at NAL and fluctuations of N_e in the altitude band 190-220 km during the interval starting
 549 at 15:44 UT; (b) PSD spectra; (c) spectral coherence; (d) phase differences.



550

551 **Figure 14: Dynamic altitude distribution of spectral coherence between EISCAT N_e and NAL b_N in 1.2-1.9 mHz frequency band at**

552 evening hours (a), and the altitude distribution of spectral coherence for the 15:44 interval.